Supplementary Materials for

Disruption of the head direction cell network impairs the parahippocampal grid cell signal

Shawn S. Winter, Benjamin J. Clark, Jeffrey S. Taube*

*Corresponding author. E-mail: jeffrey.taube@dartmouth.edu

This PDF file includes:

Materials and Methods
Figs. S1 to S12
Table S1
References

Supplementary Materials:

Materials and Methods

Subjects

We used 17 female Long-Evans rats that were divided into three groups: experiment 1, anterior thalamic nuclei (ATN) inactivation ($n = 3$); experiment 2, ATN lesion ($n = 9$), and ATN sham ($n = 5$). Rats weighed 240-340 g at the beginning of testing, and were housed singly in Plexiglas cages and maintained on a 12 hr light/dark cycle. Water and food was provided *ad libitum*. All procedures involving the rats were performed in compliance with institutional standards as set forth by the National Institutes of Health *Guide for the Care and Use of Laboratory Animals*.

Surgery

Experiment 1: Cannulation

Animals were anaesthetized with isoflurane. The animals were then fixed in a stereotaxic instrument and an incision was made to expose the skull. Animals in the inactivation group had guide cannulae surgically implanted dorsal to the ATN at coordinates relative to bregma and cortical surface: (in mm) AP: -1.5; ML: ±1.4; DV: -3.5. Small holes were drilled into the skull above the implant location, the cannulae were lowered into the brain, and the cannulae were affixed to the skull with dental acrylic.

Experiment 2: ATN lesions

Animals were anaesthetized with Nembutal (40 mg/kg, i.p.) and atropine sulfate (5 mg/kg, i.p.). The animals were then fixed in a stereotaxic instrument and an incision was made to expose the skull. Animals in the ATN lesion group had neurotoxic lesions produced by lowering a 1 µL

Hamilton syringe into the holes and infusing 0.15 µl of a 100 mM solution of N-methyl D-aspartate (NMDA; dissolved in 0.9% saline) at 4 or 6 injection sites relative to bregma and cortical surface: (in mm) AP: -1.5; ML: ±1.4; DV: -5.5; AP: -1.9; ML: ±1.4; DV: -5.5; AP: -2.3; ML: ±1.4; DV: -5.5 (last injection site was performed in only four animals). For each injection, the NMDA solution was infused at a rate of 0.05 µL/min, and the syringe was left in place for 3 min before it was slowly removed.

Electrode Implantation

All rats were surgically implanted with a moveable microdrive containing four tetrodes that was similar in design to those described in previous studies (e.g., *28*). Each tetrode was constructed by twisting together four strands of 17 µm HM-L coated platinum-iridium (90/10%) wire. The tetrodes were threaded through a 26-gauge stainless steel cannula and each wire of the tetrode bundle was connected to a pin of a Mill-Max connector. Two center pins of the connector were secured to the cannula to act as an animal ground. Three drive screws were fixed to the connector using dental acrylic creating a microdrive that was moveable in the dorsal/ventral direction (*29*). Microdrives were placed above the dorsal-caudal cortex of the right hemisphere with the intention of advancing the tetrodes through the parahippocampal cortex. After histological assessment of tetrode locations compared with previous reports (*3*), we verified that the tetrodes from all animals likely passed through layer II/III of the medial entorhinal cortex (MEC) and layer II/III of the parasubiculum (PaS)(see Fig. S1). The following coordinates were used for electrode implantation: 0.40 - 0.45 mm anterior to the transverse sinus, 4.5 - 4.6 mm lateral to lambda, and 1.5 mm below the cortical surface. Microdrives were slightly angled in the sagittal

plane (~10°), such that the tetrodes were pointing in the anterior direction. Each electrode was fixed to the skull using dental acrylic.

Procedures

Neural Screening and Recording

After 7 days of recovery from surgery, tetrodes were monitored or "screened" for cellular activity while animals foraged for 20 mg food pellets scattered on the floor of a gray square box (120 x 120 cm; 50 cm in height). The floor of the box was composed of gray photographic backdrop paper and the inside was featureless except for a white cue card attached to the wall (71 x 50 cm). The cue card was maintained at the same position throughout the experiment. A black floor-to-ceiling curtain (2.5 m in diameter) surrounded the cylinder and eight uniformly arranged lamps were located above the box to provide illumination. A color video camera was centered above the box.

To detect cell activity, electrical signals were pre-amplified by unity-gain operational amplifiers on the headstage of the animal (HS27-mini-LED or HS18-LED). The signals from tetrode wires were differentially recorded against a low activity wire from another tetrode and then bandpass filtered (600 Hz to 6 KHz) using a Digital Lynx SX (Exp. 1) or Cheetah 32 Data Acquisition System (Exp. 2). Signals that crossed a pre-set amplitude threshold (30-50 μV) were time-stamped and digitized at 32 KHz for 1 msec. Also attached to the headstage of the animal were red and green light-emitting diodes (LED) secured ~8 cm apart above the head and back of the animal, respectively. An automated video tracking system provided x- y- coordinates of each LED position at a sampling rate of 60 Hz. Local field potential was obtained from the tetrodes and was referenced to a wire from a different tetrode. Monitoring of cellular activity continued

until each of the tetrodes had been examined. If cellular activity exceeded two times the background noise level, the signals were recorded for a 20 min session. In some cases, recording sessions were cut short (10-15 min) because of technical difficulties. These sessions were included in our analysis only if the rat visited ~80% of the recording environment. If cell activity was not isolatable from background noise, the electrode array was advanced 25-50 µm and the animal was returned to its home cage and monitored a minimum of 2 hrs later.

Offline Spike Sorting

Spike sorting was conducted using graphical software. First, waveform characteristics from each tetrode were plotted as scatter plots from one of the four tetrode wires versus another wire of the same tetrode. Signal waveform characteristics such as peak amplitude, valley, energy (area of spike waveform), and height (difference between the peak and valley) were most frequently used for isolating cells. Individual units formed clusters of points in these plots and the boundaries were identified and manually "cut". Single unit isolation was further confirmed by the observation of clear refractory periods around 0 µsec in the inter-spike interval histogram. All cells with mean firing rates >10 Hz were classified as fast-spiking (putative interneurons), and the remaining units were classified as putative excitatory neurons (*S30*).

Intracranial Infusions

Lidocaine was infused into the ATN only following isolation of a grid cell. Multiple concentrations of lidocaine were used and grouped into low (8, 16, 32, 40%) and high (100%) concentrations by weight of grams/ml. The procedure began by recording a baseline 20 min session, disconnecting the animal, and returning it to their cage while data was processed to

determine if any grid cells were present. If a grid cell was identified (see criteria below), then the animal underwent the infusion process. The guide cannulae contained plugs that were the same length as the guide cannulae; these plugs were removed and infusion cannulae (33 AWG) were inserted bilaterally into the guide cannulae. Infusion cannulae protruded 0.5 to 1.0 mm ventral to the guide cannulae, depending upon previous infusion effectiveness for that animal. Infusion cannulae were connected to plastic tubing, which was connected to two Hamilton syringes mounted in an infusion pump. The pump allowed control over the flow rate and volume of the infusion. A total of 1.0 µl of lidocaine solution was infused over the course of 8 min and the cannulae were left in place for 4 min to allow diffusion of the drug. The infusion cannulae were then removed and guide cannulae were re-plugged to prevent fluid from traveling back up the guide cannulae. Immediately following the infusion, animals were connected to the recording equipment and a 20 min inactivation recording session began. Approximately 1.5 hrs following the completion of the infusion, the animal was recorded again during a recovery session. Following the recovery session the electrode was advanced 25-50 µm and the animal was not screened again until the following day. Inactivation sessions were not conducted if the drive screws had been previously turned that day, in order to ensure stable isolation across all recording sessions.

Histological analysis

At the completion of the experiment, animals were deeply anaesthetized with sodium pentobarbital and a small anodal current (20 µA, 10 sec) was passed through 2 or 3 tetrode wires from different tetrodes. The rats were then perfused intracardially with saline followed by 10% formalin solution. Each brain was removed from the skull and was post-fixed in a 10% formalin

solution containing 2% potassium ferrocyanide for at least 24 hrs. The brains were then cryoprotected in a 20% sucrose solution for at least 24 hrs and subsequently frozen. The brain was then blocked such that sections (30 μm thick) could be taken through the ATN coronally, and through the parahippocampal cortices sagitally using a cryostat. Each section was mounted on glass microscope slides, stained with thionin, and examined under light microscopy to determine the location of recording sites, location of guide cannulae implantation, and evaluate the lesions.

To quantify the extent of neurotoxic damage to the ATN, digital images were captured at 5 rostral-caudal levels through the ATN (1 mm, 1.3 mm, 1.6 mm, 1.88 mm, 2.12 mm posterior to bregma). The area of undamaged tissue in the ATN was calculated at each rostral-caudal level using Image-J software. Tissue was considered undamaged if it contained healthy neurons and few glial cells. Once the area of undamaged tissue was calculated, the area of spared tissue was summed across the sections and compared with an average area measured in sham rats. The total amount of damage was calculated using the following formula: Tissue damaged = [average area in sham rats (pixels²) - total area of spared tissue in lesioned rats (pixels²) / average area in sham rats (pixels²)] x 100%.

Recording locations were reconstructed by measuring backward from the ventral-most point made by the marking lesions to the boundaries of MEC and PaS. These measurements were matched up with screening records to identify recordings that may have fallen within each region. For experiment 1, a majority of the data were collected from MEC. Low dose cells were recorded from MEC II/III (grid = 2; HD = 2), MEC deep (grid = 38; HD = 10), and PaS II/III (grid = 15). High dose cells were recorded from MEC II/III (grid = 17; HD = 5). For experiment

2, lesion cells were recorded from MEC II/III (grid = 34), and PaS II/III (HD = 13). Sham cells were recorded from MEC II/III (grid = 48), and PaS II/III (HD = 35).

Data Analysis

Experiment 1 had a within-subjects design. To limit the number of repeat analyses upon each variable and reduce type I error rates we made direct comparison of variables of interest and adjusted our alpha level to $p < 0.01$. Analysis of session effects was done using paired-sample t-tests between baseline vs. inactivation and baseline vs. recovery. Analysis of block effects was done using an ANOVA with post-hoc pairwise comparisons against baseline (baseline 5 min block vs. inactivation block 1 through 4). When the assumption of sphericity was violated the Greenhouse-Geisser correction was used and this is reflected in the change in degrees of freedom reported in F-statements. Experiment 2 used Pearson's Chi-square tests for group comparisons of grid cell counts and the non-parametric Wilcoxon rank-sum test was used to compare grid cell and HD cell measures between groups.

HD cells

The HD of the animal was determined by the relative position of the red and green LEDs. The amount of time and number of spikes in each HD was sorted into sixty 6° bins. The firing rate for each 6° bin was determined by dividing the number of spikes by the amount of time. A firing rate by HD plot was constructed for each cell in the data set and the directionality of each cell was quantified using a number of measures. First, we computed the mean vector length (Rayleigh r-value) for each cell using circular statistics (*S31*). The mean vector length ranges between 0 and 1, with higher values indicating that spike occurrence is clustered around a

particular direction. The mean vector length was used to classify neurons either as HD cells or non-HD cells (*11, 31, 32, 33*). Cells were classified as an HD cell if its mean vector length exceeded the 95th percentile chance level generated by shuffling the neural data (*3*). Each cell (*n*=375) had its spike data randomly shuffled relative to time 400 times and the mean vector length was calculated for each iteration. The 95th percentile of the mean vector length for 150,000 iterations was 0.292, which served as the criterion for a cell to be defined as an HD cell. It is important to note that although this criterion is lower than used in previous reports (r > 0.4; *34, 35*), many HD cells in the parahippocampal region can fire over a broad range of directions (*36*), and this criterion was therefore suitable in the present study.

Grid cells

The rat's position was estimated from the red LED and was sorted into a 5 x 5 cm (25 x 25 bins) bin matrix of firing rate by time. The matrix was then subjected to smoothing using a Gaussian function (*9, 32*), which created a weighted average for each bin based on the surrounding 5 x 5 bins. Colors were associated with each bin based on their firing rate (hot colors = high firing rate; cold colors = low firing rate). From the smoothed rate maps, spatial autocorrelation maps were computed using similar methods as previous studies (*4, 37*). First, a Pearson's correlation was conducted on a cell's smoothed firing rate map, and a copy of the same rate map that was shifted to a particular x-y offset. A Pearson's correlation (*r*) was computed for all possible combinations of x-y offsets, and the resulting *r* value at each offset was entered in a new matrix. Grid cells, which fire in a triangular array spanning the entire environment, are defined by the 6-fold symmetry of the hexagon surrounding the central peak within their corresponding spatial autocorrelation maps. We quantified this symmetry by taking a circular sample of the spatial

autocorrelation map centered on the central peak, but with the central peak excluded, and computed a Pearson correlation (r) between the circular sample and its rotated copy (in 6° increments ranging from 0 to 180°). The grid score was calculated using a "moving radius" technique, in which the circular correlation was repeated multiple times varying the outer diameter of the circular sample (*3, 32*). The outer diameter was increased in steps of 1 bin from a minimum of 7 bins from the central field until it reached the edge of the autocorrelogram. For every circular sample two different grid scores were calculated. First, the difference between the highest Pearson correlations at angles of 60° or 120°, and the lowest of 30°, 90° or 150° was taken as a traditional grid score (*4*). Second, the Pearson correlation for every 6° increment ranging from 0 to 180° was fit to a sinusoid curve, and the fit of this sinusoid curve was taken as the sinusoid-grid score. The traditional grid score measure was susceptible to false detects of cells with high grid scores whose spatial autocorrelograms did not evoke a good hexagonal pattern, and these cells should not be classified as grid cells. Thus, we created the sinusoid-grid measure to reduce these false detects. For experiment 1, the inactivation experiment, grid cells were identified based on their strict periodic hexagonal firing fields and the experiment only proceeded if a grid cell had been identified within the population of cells recorded for that session. Grid cells were visually identified based on the observation of several distinct firing fields arranged in a hexagonal pattern. The grid cells identified for experiment 1 had a mean grid score of 0.754 ± 0.192 and ranged from 0.245 to 0.941. For experiment 2, because all cellular signals were recorded throughout the dorso-ventral extent of the parahippocampal cortex for each animal, we created an objective criterion for a cell to be classified as a grid cell. Similar to previous studies (e.g., *3, 9*), we classified a cell as a grid cell only if its grid score exceeded the 95th percentile (or 99th percentile in an additional analysis, see Fig. S3) chance level generated by

shuffling the neural data. Each cell (*n*=375) had its spike data randomly shuffled relative to time

100 times and a sinusoid-grid score was calculated for each iteration. The 95th percentile for the

sinusoid-grid score of the 37,500 iterations was 0.439.

Signal change score

We sought to compute a measure that could directly compare grid score change to HD mean

vector length change across simultaneously recorded grid and HD cells to determine if both

signals are modulated similarly. First we generated two cross-correlations between

baseline/inactivation and baseline/recovery for each cell. For grid cells we cross-correlated the

25 x 25 bin array spanning the entire environment, and for HD cells we cross-correlated the 60

bin array spanning all 360° of the environment. Because the cross-correlation is highly variable

between grid and HD cells and between individuals cells because of isolation or signal quality

we took the difference score between cross-correlations: baseline/recovery-baseline/inactivation.

This was done to generate a degree of change between a good signal comparison

(baseline/recovery) and inactivation comparison. Next, we averaged all grid cell change scores

per recording session (ΔGrid) and HD cell change scores per recording session (ΔHD) to

generate a signal change per recording session. Finally, we correlated ΔGrid and ΔHD using

Spearman's Rho (r_s) to assess the relationship between these two variables.

Theta rhythm

Theta rhythmicity was computed from the local field potential in two ways. First, we computed a

power spectrum using the Matlab spectrogram function which conducts a fourier transform on

the signal using a Hanning window with a resolution of 1 Hz between the range of 0 to 20 Hz in

0.25 Hz steps. The power reported by the spectrogram function between 6-10 Hz was taken as the raw theta power. All sessions and blocks were then normalized by dividing the power of each session or block by the mean baseline power. Theta power is influenced by running speed which was significantly influenced during the beginning of the high inactivation session. In order to control for changes in LFP that were caused by differences in running speed we calculated theta rhythmicity using a theta ratio. Theta ratio is the ratio of theta power (6-10 Hz) to delta power (2-4 Hz) from the spectrogram.

Results

When data are illustrated supplemental results are reported in the accompanying figure captions.

We assessed theta rhythmicity in high dose cells by computing the depth of modulation within spike timing autocorrelograms. Rhythmicity was analyzed only if a sinusoid within theta rhythm fit the autocorrelation curve >0.2. Fits below this threshold were deemed too low to be considered rhythmically modulated. There was no effect of lidocaine upon grid cell rhythmicity at low (baseline: 0.349 ± 0.019; low: 0.373 ± 0.029; $t_{(33)} = 0.829$, n.s.) or high (baseline: 0.402 ± 0.027; high: 0.457 ± 0.079; $t_{(8)} = 0.696$, n.s.) doses. There was no effect of lidocaine upon HD cell rhythmicity at low (baseline: 0.410 ± 0.043; low: 0.384 ± 0.086; $t_{(3)} = 0.535$, n.s.) or high (baseline: 0.442 ± 0.009; high: 0.426 ± 0.075; $t_{(2)} = 0.203$, n.s.) doses. When spiking occurred in principle cells it maintained its theta rhythmicity.
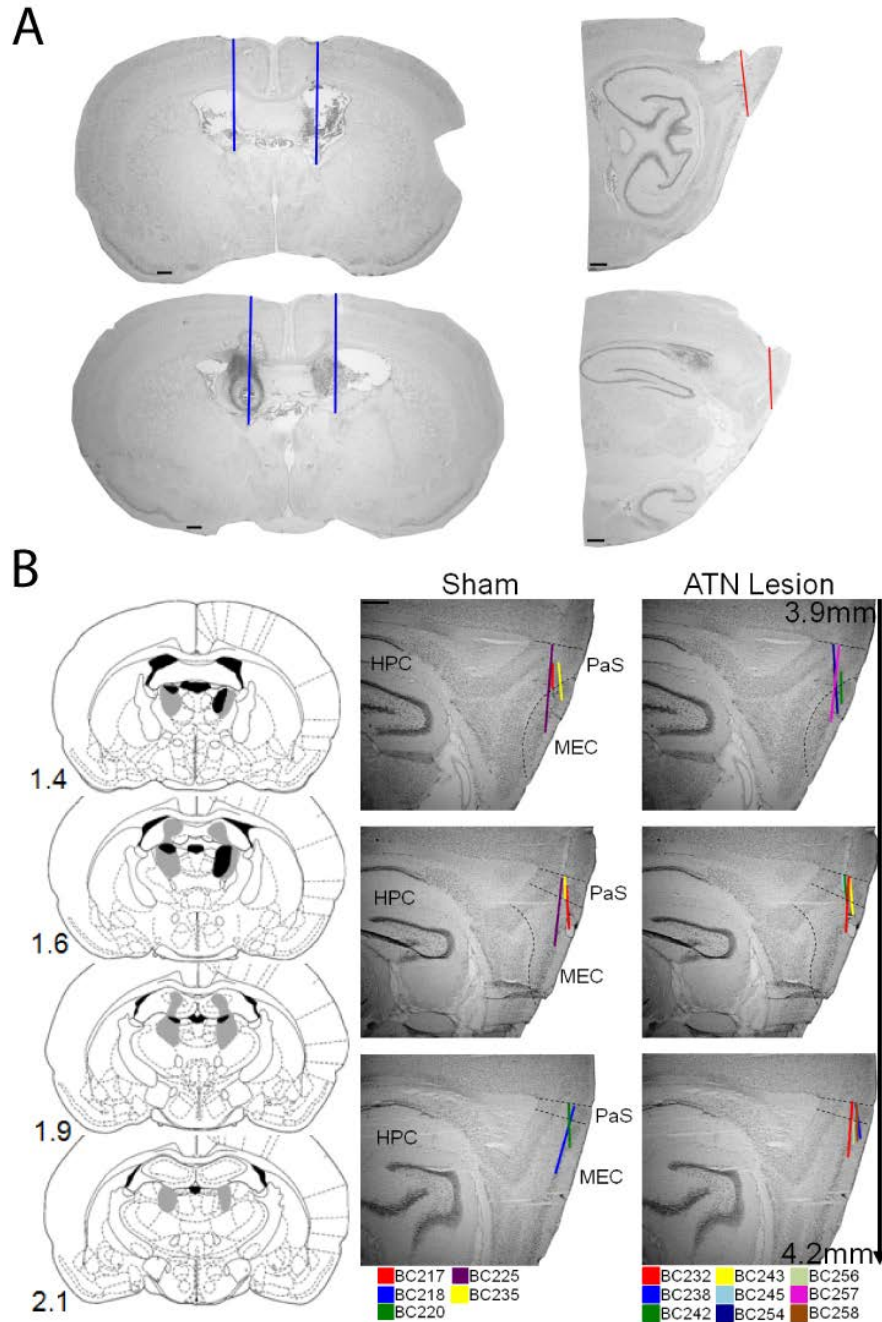
Fig. S1: (A) Experiment 1: cannulae placement (blue line) in the ATN (left) and electrode track (red line) through the parahippocampal cortex (right). (B) Experiment 2: selected plates from Paxinos and Watson (1998) showing the rostral-caudal extent of ATN lesions at relative coordinates from bregma (left). The extent of the largest (gray) and smallest (black) lesion is shown. Sagittal sections showing the tetrode trajectories through the parahippocampal cortex for sham (middle) and ATN lesion (right) animals. Each color indicates the tetrode trajectory from an individual animal. Scale bars = 0.5 mm.
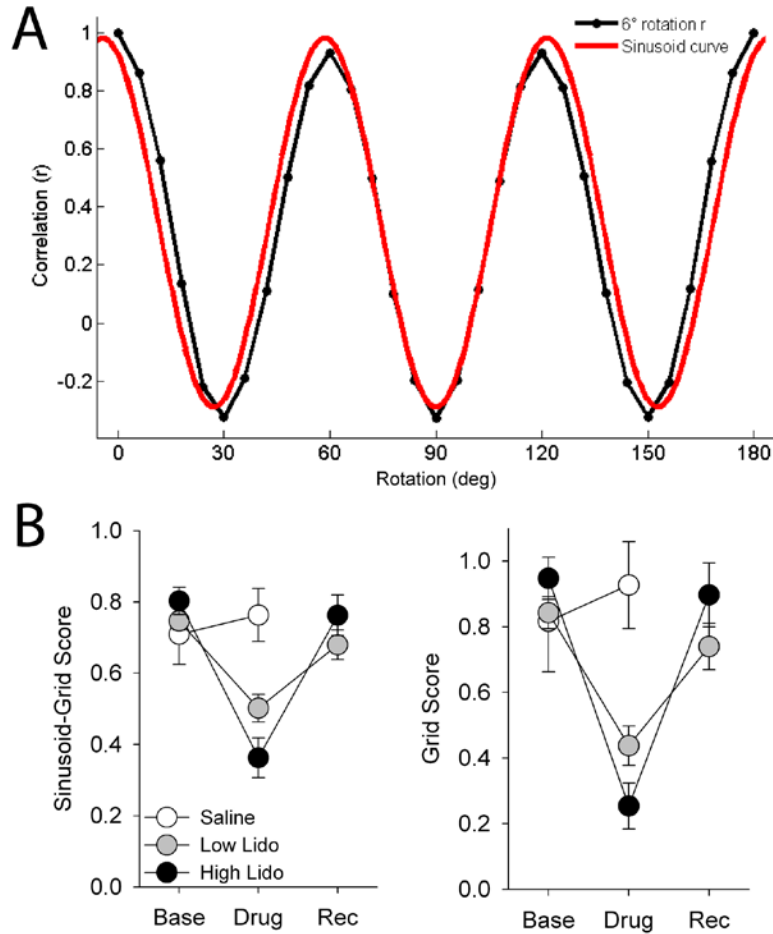
Fig. S2: (A) Illustration of sinusoid-grid score calculation. Correlations are generated between an annulus from the autocorrelation map with the center grid node and peripheral grid nodes removed and 6° rotations of the annulus around the center (black dots and line) up to 180°. Then a sinusoid curve (red line) is fit to the 31 data points in Matlab using the curve-fit toolbox fourier1 function with the curve fixed at 6 Hz frequency to assess for the hexagonal frequency exhibited by a grid cell. The fit between the 31 rotations at 6° and the sinusoid curve is the reported sinusoid-grid score. Illustrated cell measures: sinusoid-grid: 0.932; traditional grid score: 1.356. (B) Data for experiment 1 sinusoid-grid score (left) and traditional grid score (right) illustrated side-by-side to demonstrate the correlation between the two different measures ($r = 0.933$). The relationship between sinusoid-grid and traditional grid scores decreases ($r = 0.830$), but is still high for cells visually identified as non-grid cells.
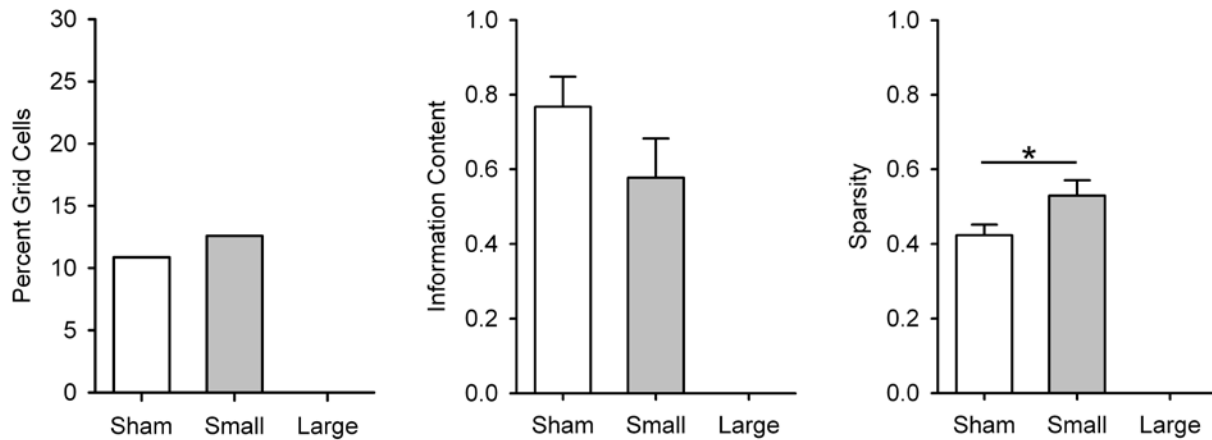
Fig. S3: Data for percentage of grid cells (left), information content (bits/spike)(middle), and sparsity (right) measures for cells that had grid score values greater than the 99th percentile of the shuffled distribution of grid scores (criteria = 0.568). Using the 95th percentile was a liberal inclusion criterion selected to ensure inclusion of as many grid and grid-like cells as possible, given the continuum of grid firing in these regions. This procedure was done because ATN lesions disrupted location-based firing characteristics at the 95th percentile and we wanted to include as much grid-like firing as possible to illustrate the effects of lesions. When the more conservative 99th percentile was used it eliminated a large number of grid-like cells that do not have strong symmetrical firing patterns compared to traditional grid cells. A high criterion will also reduce the number of non-grid cells falsely detected as grid cells in all groups. As a result, none of the cells recorded in the large lesion group passed the grid score criterion ($\chi^2(1) = 5.56$, $p < 0.05$). In animals with small ATN lesions there were comparable number of grid cells (sham 10.9%; small lesion 12.6%), information content was moderately lower ($W = 307$, $p = 0.09$) and sparsity was significantly higher ($W = 465$, $p < 0.05$). Significance level: * = p < 0.05.
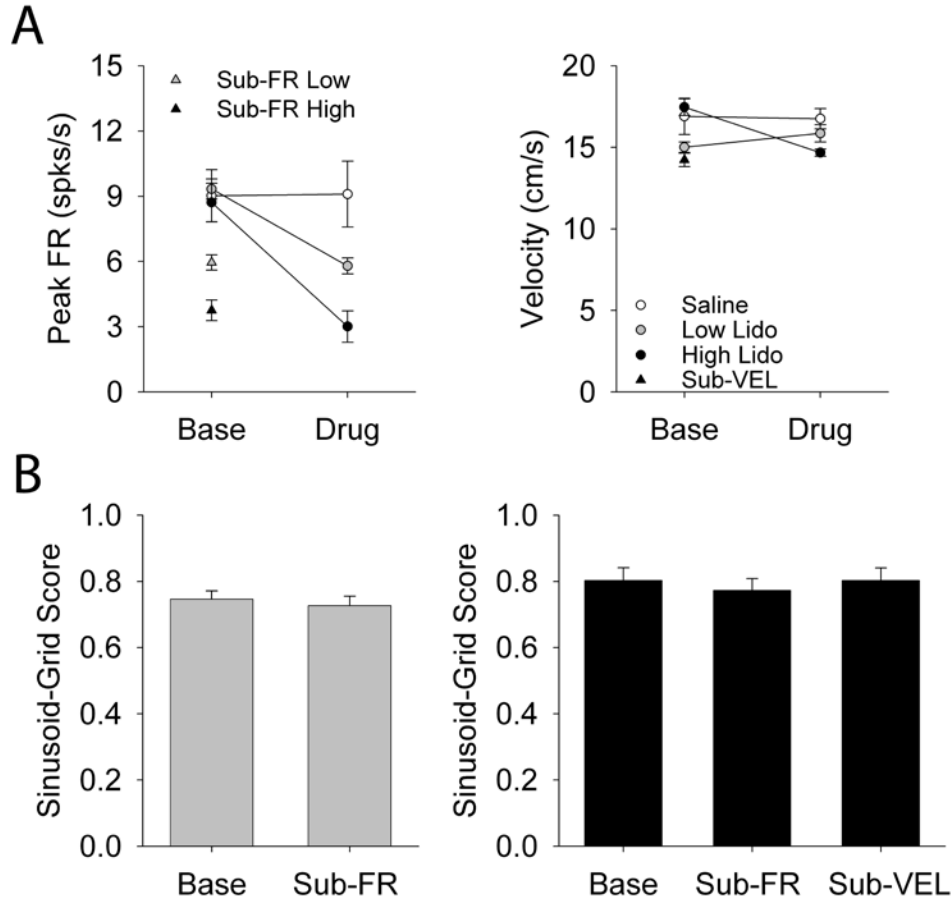
Fig. S4: Data for (**A**) peak firing rate (left) and linear velocity (right), and (**B**) sinusoid-grid score for low (left) and high (right) concentration lidocaine that is comparing sub-sampled data against baseline. Lidocaine produced a significant decrease in peak firing rates at low and high concentrations. We randomly sub-sampled spikes during the baseline session to determine if firing rate decreases could account for the observed reduction in grid scores during inactivation. There was no significant difference in grid scores between baseline and sub-sampled firing rate (Sub-FR) for low ($n = 55$ cells; baseline: 0.746 ± 0.025; sub-FR: 0.727 ± 0.029; $t_{(54)} = 1.163$, n.s.) or high ($n = 17$ cells; baseline: 0.803 ± 0.038; sub-FR: 0.773 ± 0.035; $t_{(16)} = 1.039$, n.s.) concentrations of lidocaine. Lidocaine produced a significant decrease in mean movement velocity at high (baseline: 17.46 ± 0.51; drug: 14.67 ± 0.22; $t_{(6)} = 4.646$, $p < 0.01$), but not low (baseline: 15.01 ± 0.32; drug: 15.86 ± 0.53; $t_{(17)} = 1.664$, n.s.) doses of lidocaine. We sub-sampled movement above the mean velocity during the high concentration baseline session to determine if velocity reductions could account for the observed decrease in grid scores during inactivation. There was no significant difference in grid scores between baseline and sub-sampled velocity (sub-VEL; baseline: 0.803 ± 0.038; sub-VEL: 0.803 ± 0.038; $t_{(16)} = 0.109$, n.s.). These results provide evidence that a decrease in firing rate or movement velocity observed during inactivation session is not the primary cause of decreased grid scores observed during the inactivation session.
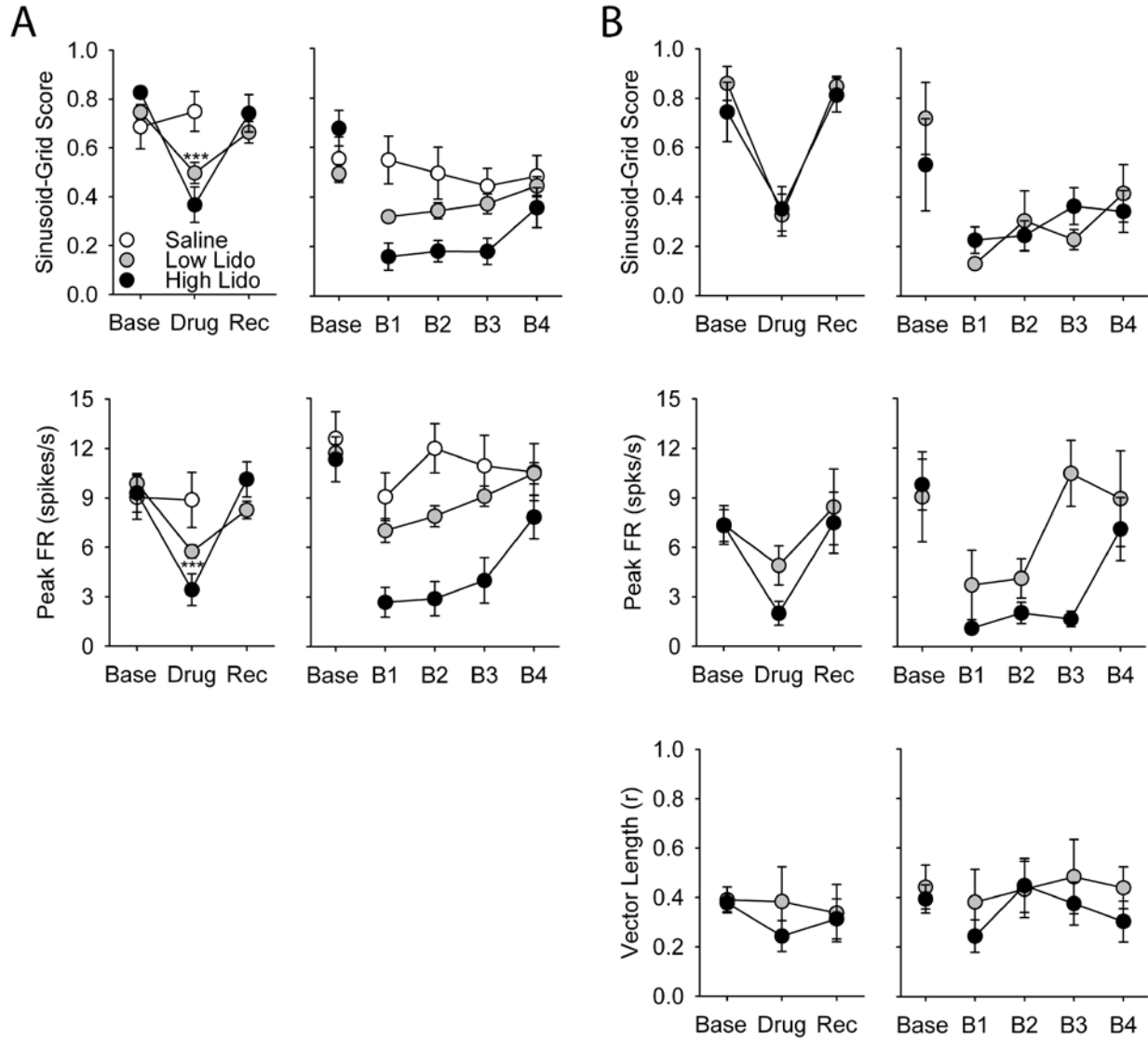
Fig. S5: Data for inactivation effects upon (**A**) grid and (**B**) conjunctive grid x HD cell sinusoidal-grid score (top), peak firing rate (middle), and mean vector length (bottom) measures. Previous analyses assessed the effect of lidocaine inactivation upon grid or HD signals independent of cell type. To determine if inactivation of ATN disproportionally influenced conjunctive cells by disrupting the HD component, but leaving grid signals spared, we analyzed each measure by cell type. The results for grid-only cells (i.e., not including grid x HD conjunctive cells) were identical to results reported in the main text for grid signals. There was a low number of conjunctive cells (low: *n* = 3; high: *n* = 5), but their data follow the same trends observed in grid and HD signals from the main text.
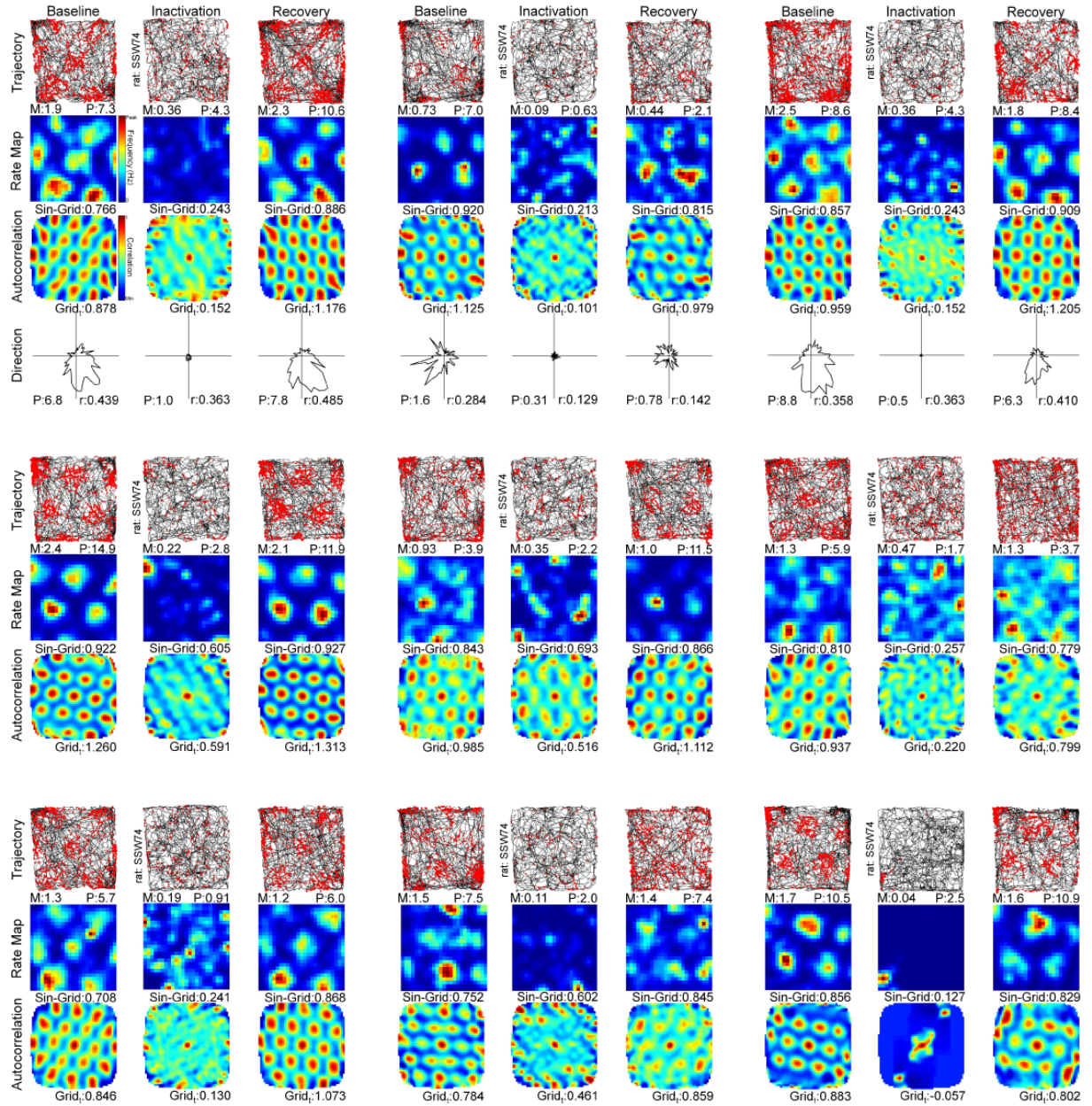
Fig. S6 (page 1 of 2): Examples of all high lidocaine inactivation upon conjunctive grid x HD (left) and grid-only (middle and right) cells. Rows and columns are the same from previous figures. Sin-Grid = sinusoid-grid score. $Grid_t$ = traditional grid score. Note the example in the bottom right is the same cell illustrated in Fig. 1.
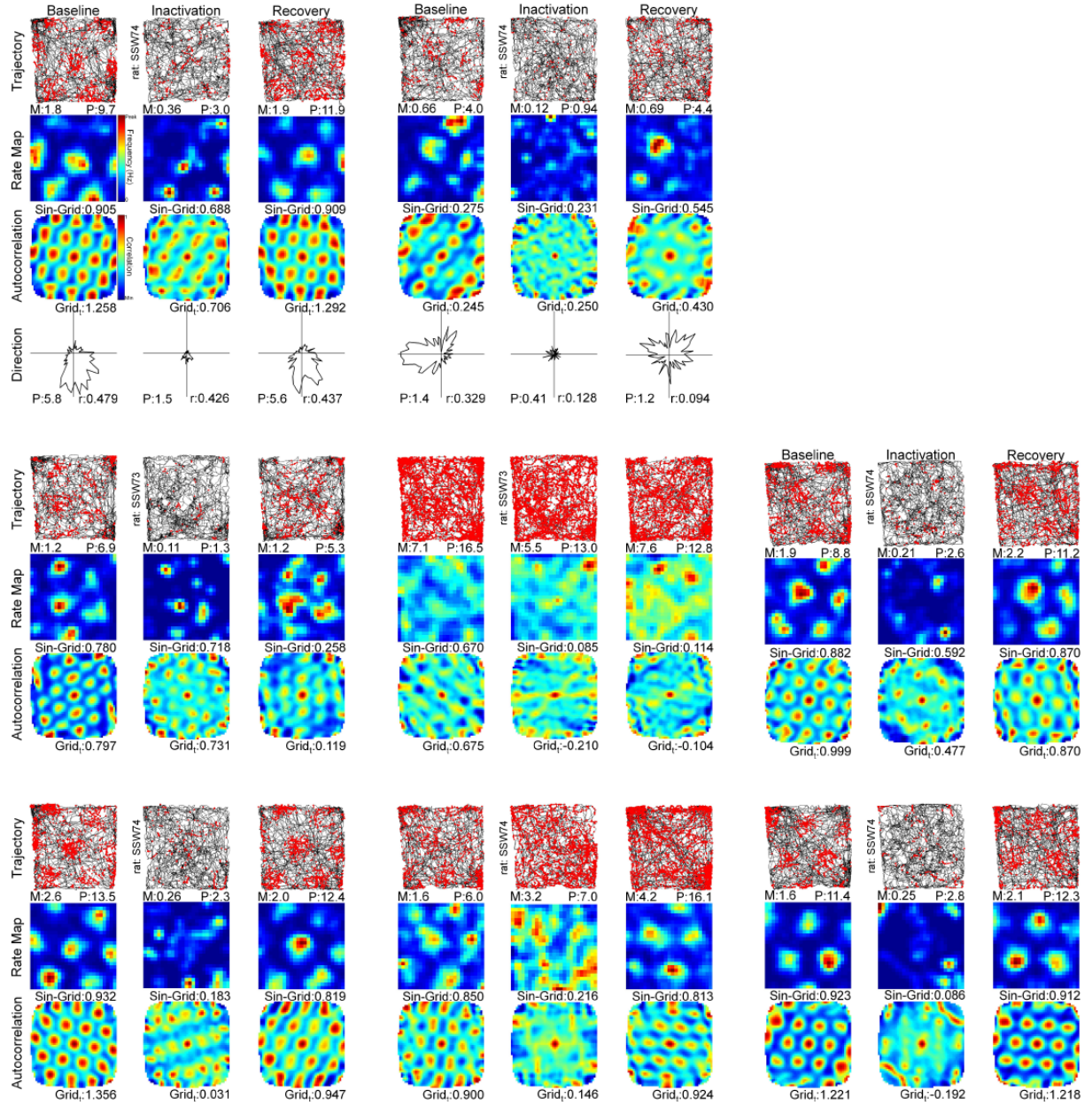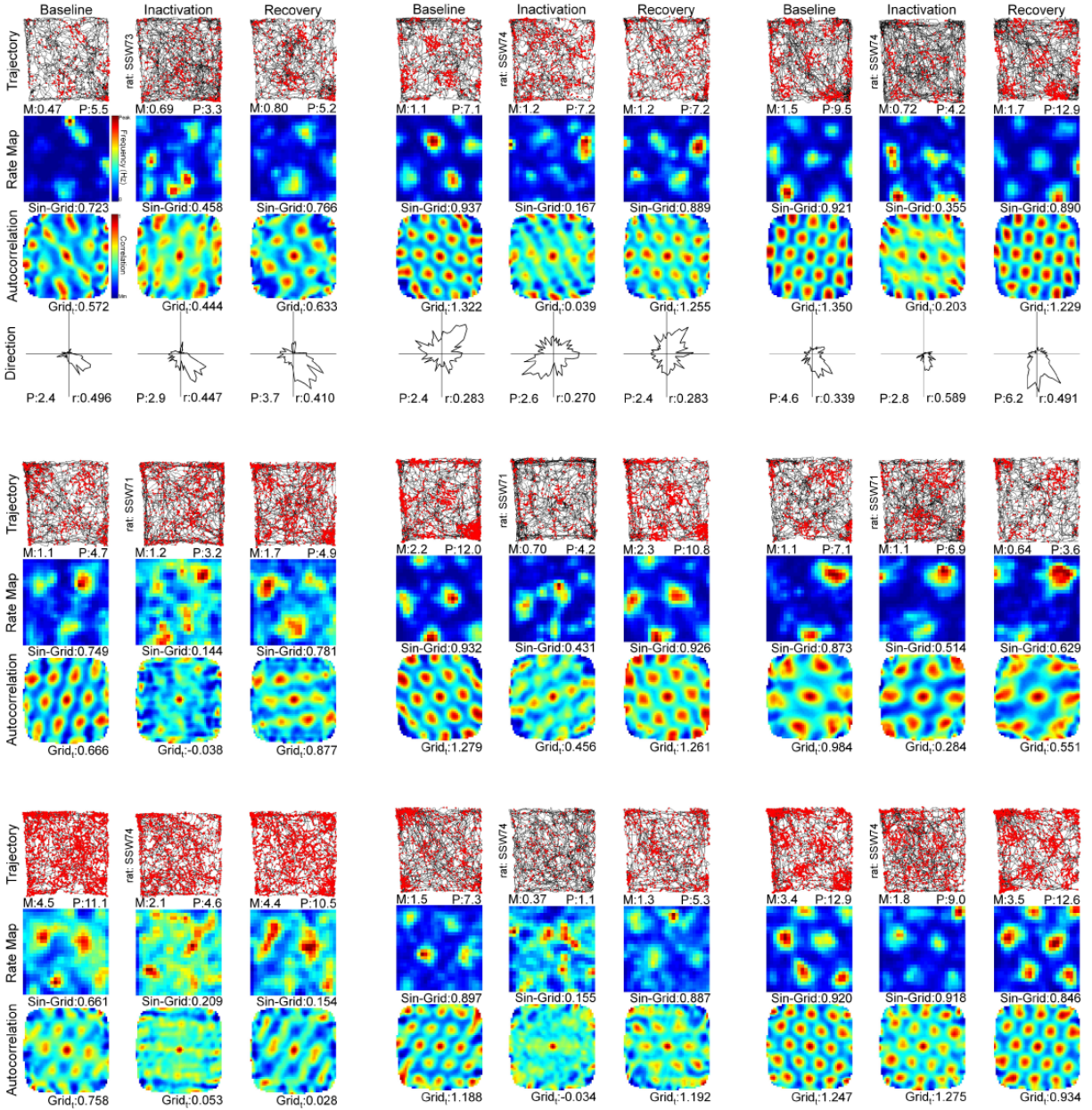
Fig. S6 (page 2 of 2)

Fig. S7 (page 1 of 2): Examples of 18 low lidocaine inactivation upon conjunctive grid x HD (top row) and grid-only cells. Rows and columns are the same from previous figures.
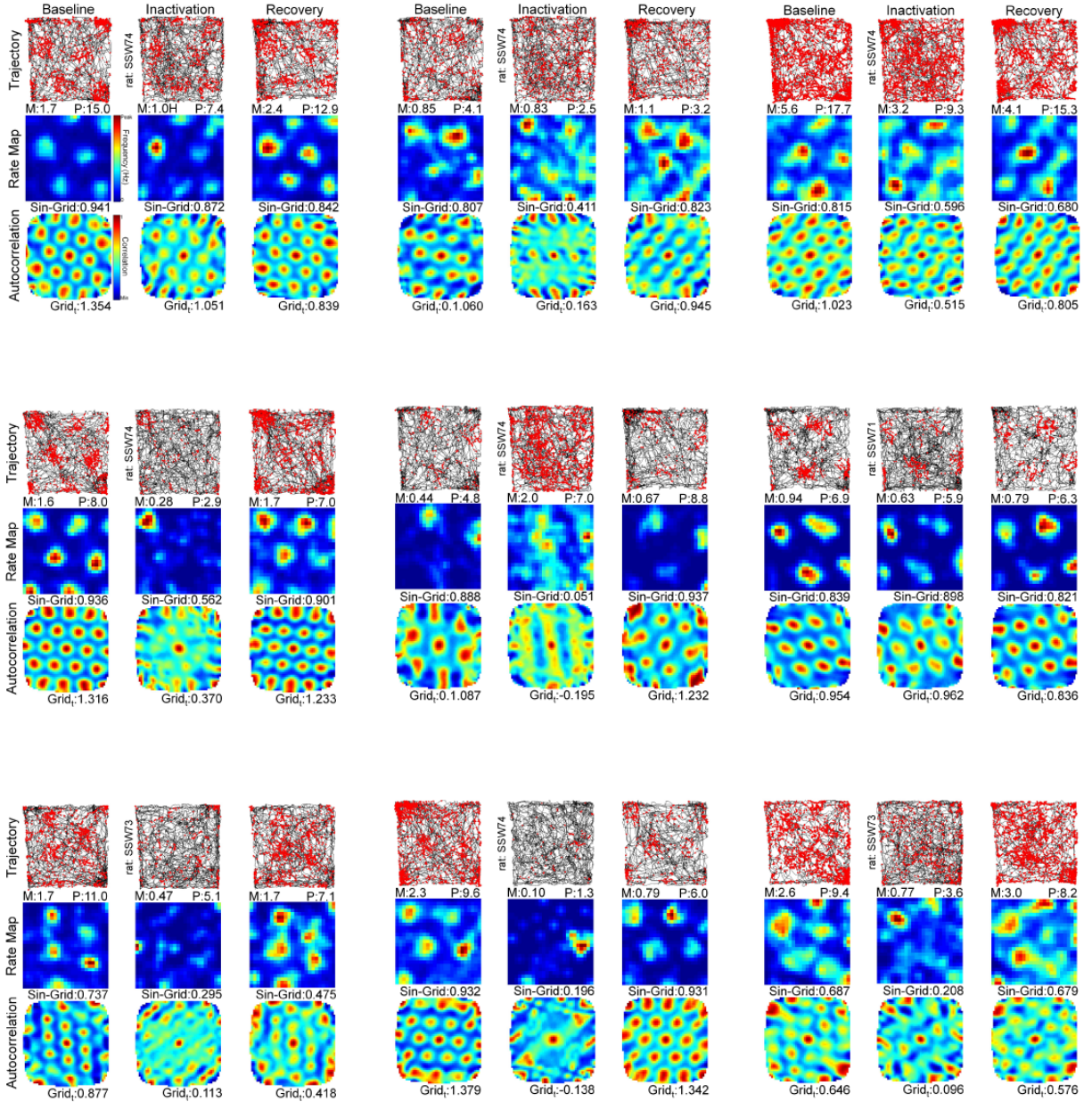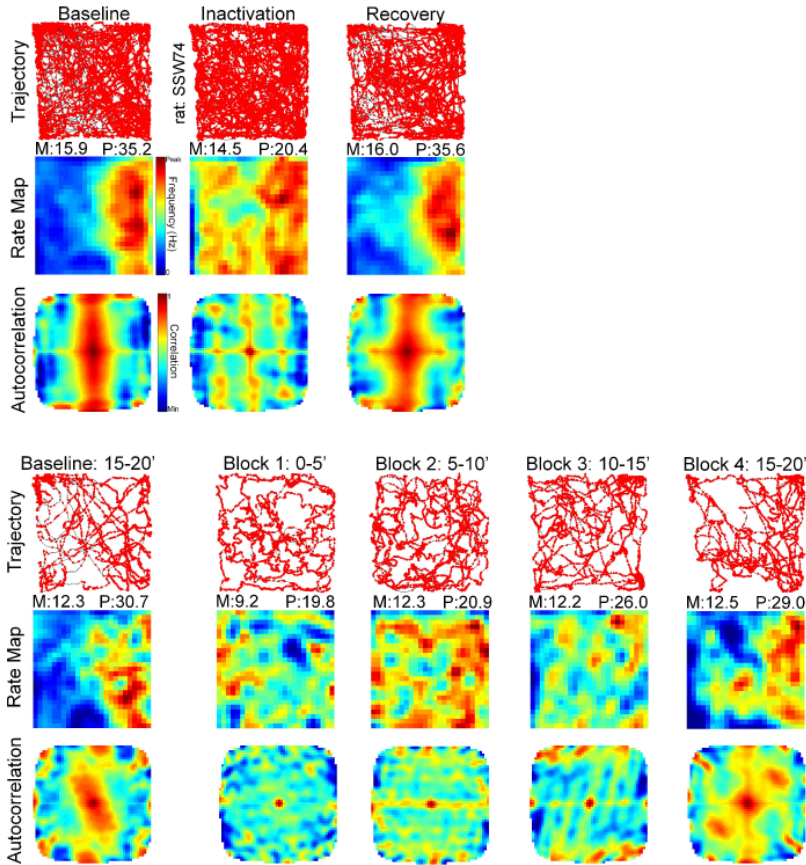
Fig. S7 (page 1 of 2)

Fig. S8: Example of a border cell response to low dose (40%) lidocaine infusion across sessions (top) and blocks (bottom). Rows and columns are the same from previous figures. ATN inactivation appears to disrupt border related firing patterns during the inactivation session and they begin to return during the final block of the inactivation session.
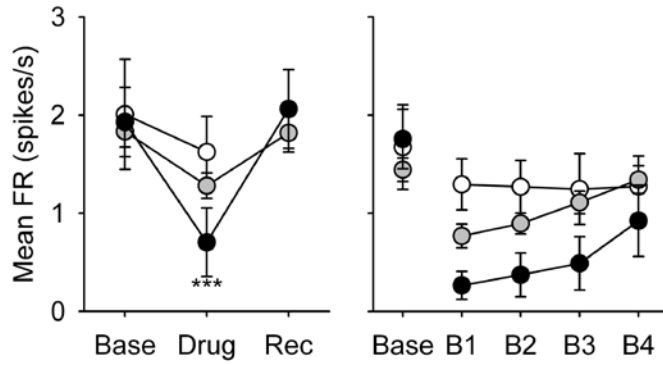
Fig. S9: Data for grid cell mean firing rate across sessions (left) and blocks (right). Mean firing rate had the same pattern of results as peak firing rate. Mean firing rate was significantly decreased by lidocaine infusions at low doses (baseline: 1.83 ± 0.16; low inactivation: 1.28 ± 0.13; $t_{(54)} = 4.993$, $p < 0.001$) and high doses (baseline: 1.93 ± 0.35; high inactivation: 0.70 ± 0.35; $t_{(16)} = 5.485$, $p < 0.001$), and recovered within approximately 1.5 hours (low recovery: 1.82 ± 0.20; $t_{(34)} = 1.148$, n.s.; high recovery: 2.06 ± 0.40; $t_{(16)} = 0.753$, n.s.). Low doses significantly impaired mean firing rates for the first three blocks and recovered by the last block (low baseline 5 min: 1.44 ± 0.12; $F_{(2.134,115.217)} = 13.616$, $p < 0.001$; low inactivation block 1: 0.77 ± 0.12, $p < 0.001$; block 2: 0.90 ± 0.11, $p < 0.001$; block 3: 1.11 ± 0.12, $p < 0.010$; block 4: 1.34 ± 0.14, n.s.). High doses significantly impaired mean firing rates for the first three blocks and recovered by the last block (high baseline 5 min: 1.76 ± 0.30; $F_{(1.927,30.835)} = 20.970$, $p < 0.001$; high inactivation block 1: 0.27 ± 0.14, $p < 0.001$; block 2: 0.37 ± 0.22, $p < 0.001$; block 3: 0.49 ± 0.27, $p < 0.001$; block 4: 0.92 ± 0.36, n.s.).
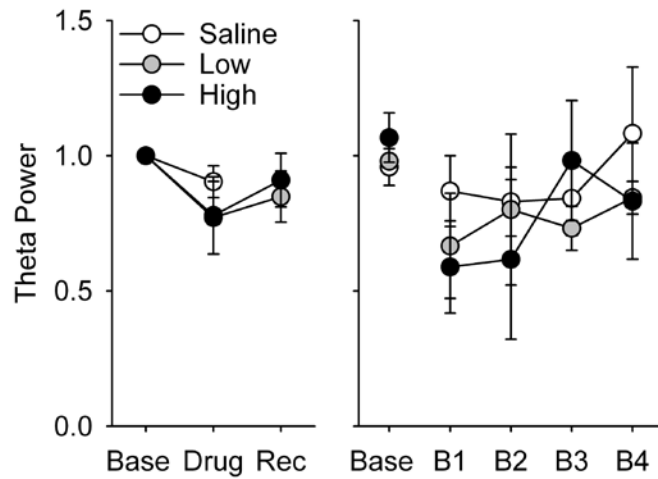
Fig. S10: Data for normalized theta power in the LFP across sessions (left) and blocks (right). There was no significant effect of lidocaine upon normalized theta power at low doses across sessions (low baseline: 1.0; low inactivation: 0.771 ± 0.134; $t_{(17)} = 1.709$, n.s.) or blocks (low baseline: 0.980 ± 0.026; $F_{(1.229, 20.892)} = 0.836$, n.s.; low block 1: 0.667 ± 0.194; low block 2: 0.801 ± 0.279; low block 3: 0.732 ± 0.082; low block 4: 0.845 ± 0.061). There was no significant effect of lidocaine upon normalized theta power at high doses across sessions (high baseline: 1.0; high inactivation: 0.779 ± 0.143; $t_{(6)} = 1.545$, n.s.) or blocks (high baseline: 1.067 ± 0.091; $F_{(4,24)} = 1.342$, n.s.; high block 1: 0.589 ± 0.170; high block 2: 0.617 ± 0.296; high block 3: 0.982 ± 0.222; high block 4: 0.832 ± 0.215). Although there was no significant difference in theta power, there was a decrease in the first two blocks for the high dose group. This drop in normalized theta power is likely related to an observed decrease in movement velocity during the inactivation session in the high dose (see Fig. S4). Velocity has been linked to changes in theta power; however, this small change in theta power is unlikely the cause of the decreased grid scores because 1) theta ratio was spared indicating that it was not a selective change to theta rhythmicity but rather to the overall LFP, 2) sub-sampling movement velocity during baseline to match the inactivation session did not influence grid scores (Fig. S4), 3) theta power is equivalent to baseline during the final half of the inactivation session while grid scores remain significantly reduced for high concentrations, and 4) theta power is not influenced during the low concentrations when grid scores are significantly decreased.
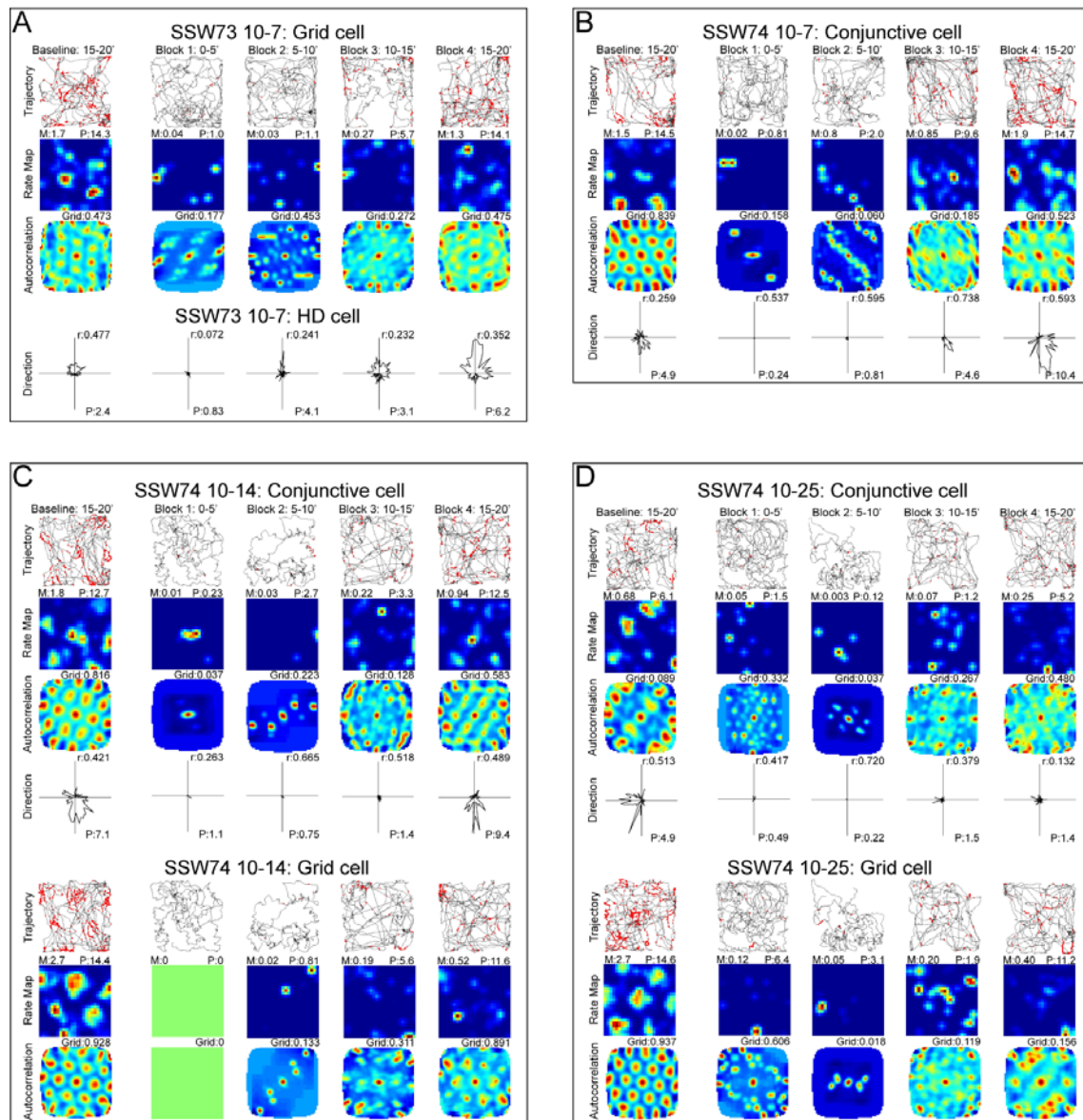
Fig. S11: Examples of lidocaine inactivation upon (**A**) a simultaneously recorded HD cell and a grid cell (low dose lidocaine), (**B**) a conjunctive grid x HD cell (low dose lidocaine), and (**C** and **D**) simultaneously recorded grid x HD conjunctive cells and grid-only cells (high dose lidocaine). Rows and columns are the same from previous figures. Sin-Grid = sinusoid-grid score. Grid$_t$ = traditional grid score. In (A) HD cell firing is gradually returning during Blocks 3 and 4 at the same time that grid cell firing is steadily improving. In (B) the grid cell signal is not fully restored until the HD signal has fully returned in Block 4. In (C) the grid signal for both cells is not restored until the HD signal in the conjunctive cell is fully recovered in Block 4. In (D) the HD signal has not recovered by Block 4 in the conjunctive cell and neither of the grid cell signals have yet recovered. In summary, for each of these four examples, the presence or absence of the grid cell signal follows the time course of the robustness in the HD signal.
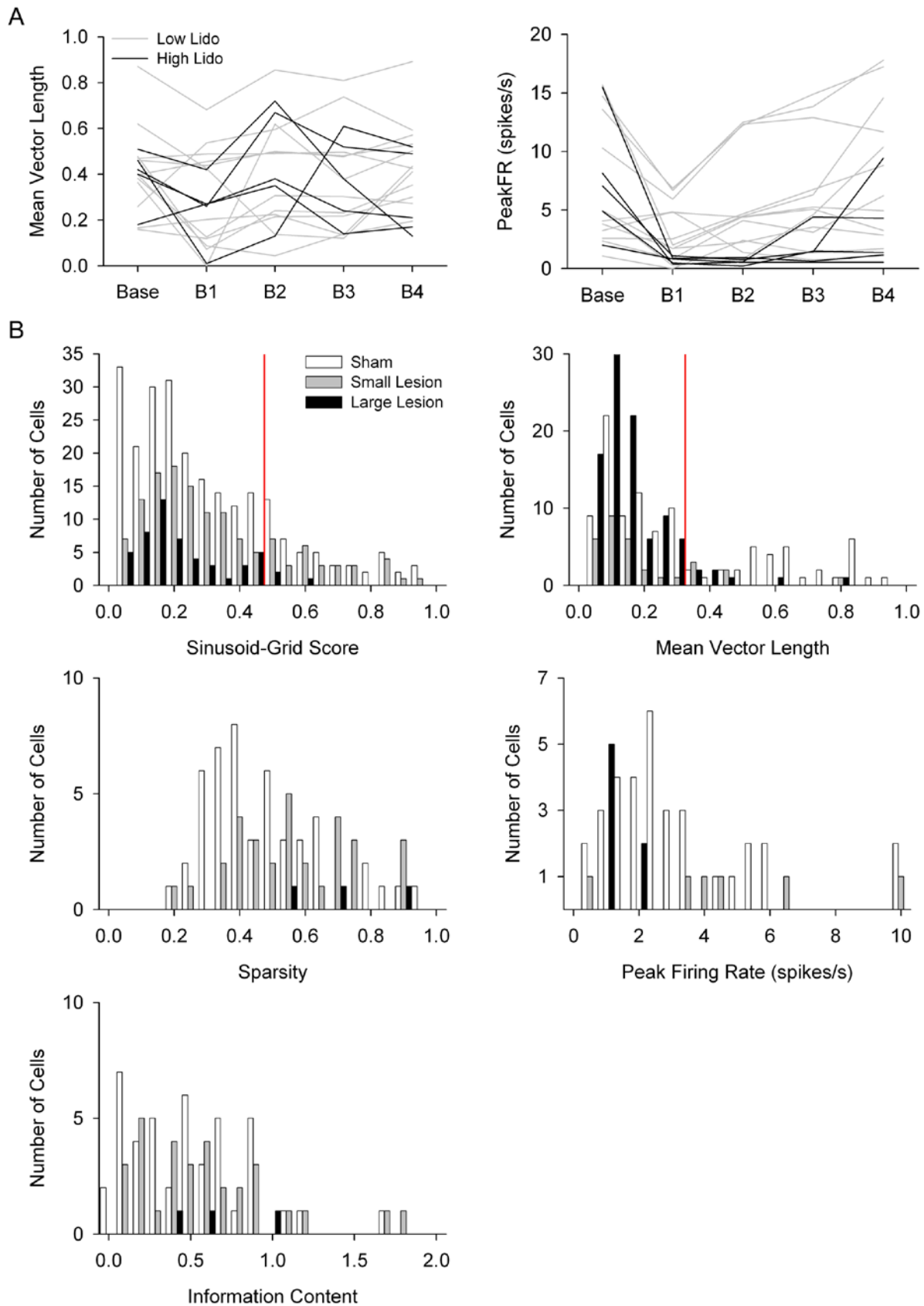
Fig. S12: (**A**) Experiment 1 individual cell data of inactivation across blocks for HD cell mean vector length (left) and peak firing rate (right) As mentioned in the manuscript, the mean vector length parameter is not a good measure for the robustness of the directional signal in this case because firing rates have dropped precipitously. Reduced firing rates can lead to the erroneous impression that the directional signal is still evident. (**B**) Experiment 2 histograms of grid and HD cell data. All cells' sinusoid-grid score (top left), and grid cell sparsity (middle left) and information content (bottom left). All cells' mean vector length (top right) and HD cell peak firing rate (bottom right). Red line indicates 95th percentile criterion.

Table S1. Number of cells recorded under each condition by individual rats.

Cell type	Concentration	SSW71	SSW73	SSW74
Grid	Saline	0	3	7
	Low	15	18	22
	High	0	2	15
HD	Saline	0	0	2
	Low	2	8	2
	High	0	0	5

References

1. E. I. Moser, E. Kropff, M.-B. Moser, Place cells, grid cells, and the brain's spatial representation system. *Annu. Rev. Neurosci.* **31**, 69–89 (2008). [Medline](doi:10.1146/annurev.neuro.31.061307.090723) doi:10.1146/annurev.neuro.31.061307.090723

2. J. S. Taube, The head direction signal: Origins and sensory-motor integration. *Annu. Rev. Neurosci.* **30**, 181–207 (2007). Medline doi:10.1146/annurev.neuro.29.051605.112854

3. C. N. Boccara, F. Sargolini, V. H. Thoresen, T. Solstad, M. P. Witter, E. I. Moser, M. B. Moser, Grid cells in pre- and parasubiculum. *Nat. Neurosci.* **13**, 987–994 (2010). Medline doi:10.1038/nn.2602

4. T. Hafting, M. Fyhn, S. Molden, M.-B. Moser, E. I. Moser, Microstructure of a spatial map in the entorhinal cortex. *Nature* **436**, 801–806 (2005). Medline doi:10.1038/nature03721

5. N. Burgess, C. Barry, J. O'Keefe, An oscillatory interference model of grid cell firing. *Hippocampus* **17**, 801–812 (2007). Medline doi:10.1002/hipo.20327

6. M. E. Hasselmo, L. M. Giocomo, E. A. Zilli, Grid cell firing may arise from interference of theta frequency membrane potential oscillations in single neurons. *Hippocampus* **17**, 1252–1271 (2007). Medline doi:10.1002/hipo.20374

7. B. L. McNaughton, F. P. Battaglia, O. Jensen, E. I. Moser, M.-B. Moser, Path integration and the neural basis of the 'cognitive map'. *Nat. Rev. Neurosci.* **7**, 663–678 (2006). Medline doi:10.1038/nrn1932

8. M. P. Brandon, A. R. Bogaard, C. P. Libby, M. A. Connerney, K. Gupta, M. E. Hasselmo, Reduction of theta rhythm dissociates grid cell spatial periodicity from directional tuning. *Science* **332**, 595–599 (2011). Medline doi:10.1126/science.1201652

9. J. Koenig, A. N. Linder, J. K. Leutgeb, S. Leutgeb, The spatial periodicity of grid cells is not sustained during reduced theta oscillations. *Science* **332**, 592–595 (2011). Medline doi:10.1126/science.1201685

10. F. Raudies, M. P. Brandon, G. William Chapman, M. E. Hasselmo, Head direction is coded more strongly than movement direction in a population of entorhinal neurons. *Brain Res.* (2014). 10.1016/j.brainres.2014.10.053 Medline doi:10.1016/j.brainres.2014.10.053

11. J. P. Bassett, M. L. Tullman, J. S. Taube, Lesions of the tegmentomammillary circuit in the head direction system disrupt the head direction signal in the anterior thalamus. *J. Neurosci.* **27**, 7564–7577 (2007). Medline doi:10.1523/JNEUROSCI.0268-07.2007

12. J. P. Goodridge, J. S. Taube, Interaction between the postsubiculum and anterior thalamus in the generation of head direction cell activity. *J. Neurosci.* **17**, 9315–9330 (1997). Medline

13. J. S. Taube, Head direction cells recorded in the anterior thalamic nuclei of freely moving rats. *J. Neurosci.* **15**, 70–86 (1995). Medline

14. M. Tsanov, E. Chah, S. D. Vann, R. B. Reilly, J. T. Erichsen, J. P. Aggleton, S. M. O'Mara, Theta-modulated head direction cells in the rat anterior thalamus. *J. Neurosci.* **31**, 9489–9502 (2011). Medline doi:10.1523/JNEUROSCI.0353-11.2011

15. Materials and methods are available as supporting materials on *Science* Online.

16. A. Burgalossi, L. Herfst, M. von Heimendahl, H. Förste, K. Haskic, M. Schmidt, M. Brecht, Microcircuits of functionally identified neurons in the rat medial entorhinal cortex. *Neuron* **70**, 773–786 (2011). [Medline](#) [doi:10.1016/j.neuron.2011.04.003](#)

17. T. Bonnevie, B. Dunn, M. Fyhn, T. Hafting, D. Derdikman, J. L. Kubie, Y. Roudi, E. I. Moser, M. B. Moser, Grid cells require excitatory drive from the hippocampus. *Nat. Neurosci.* **16**, 309–317 (2013). [Medline](#) [doi:10.1038/nn.3311](#)

18. A. Terrazas, M. Krause, P. Lipa, K. M. Gothard, C. A. Barnes, B. L. McNaughton, Self-motion and the hippocampal spatial metric. *J. Neurosci.* **25**, 8085–8096 (2005). [Medline](#) [doi:10.1523/JNEUROSCI.0693-05.2005](#)

19. A. C. Welday, I. G. Shlifer, M. L. Bloom, K. Zhang, H. T. Blair, Cosine directional tuning of theta cell burst frequencies: Evidence for spatial coding by oscillatory interference. *J. Neurosci.* **31**, 16157–16176 (2011). [Medline](#) [doi:10.1523/JNEUROSCI.0712-11.2011](#)

20. E. J. Golob, J. S. Taube, Head direction cells and episodic spatial information in rats without a hippocampus. *Proc. Natl. Acad. Sci. U.S.A.* **94**, 7645–7650 (1997). [Medline](#) [doi:10.1073/pnas.94.14.7645](#)

21. E. C. Warburton, J. P. Aggleton, Differential deficits in the Morris water maze following cytotoxic lesions of the anterior thalamus and fornix transection. *Behav. Brain Res.* **98**, 27–38 (1999). [Medline](#) [doi:10.1016/S0166-4328(98)00047-3](#)

22. R. J. Frohardt, J. P. Bassett, J. S. Taube, Path integration and lesions within the head direction cell circuit: Comparison between the roles of the anterodorsal thalamus and dorsal tegmental nucleus. *Behav. Neurosci.* **120**, 135–149 (2006). [Medline](#) [doi:10.1037/0735-7044.120.1.135](#)

23. C. Parron, B. Poucet, E. Save, Entorhinal cortex lesions impair the use of distal but not proximal landmarks during place navigation in the rat. *Behav. Brain Res.* **154**, 345–352 (2004). [Medline](#) [doi:10.1016/j.bbr.2004.03.006](#)

24. C. Parron, E. Save, Evidence for entorhinal and parietal cortices involvement in path integration in the rat. *Exp. Brain Res.* **159**, 349–359 (2004). [Medline](#) [doi:10.1007/s00221-004-1960-8](#)

25. S. S. Winter, J. R. Köppen, T. B. N. Ebert, D. G. Wallace, Limbic system structures differentially contribute to exploratory trip organization of the rat. *Hippocampus* **23**, 139–152 (2013). [Medline](#) [doi:10.1002/hipo.22075](#)

26. E. J. Golob, J. S. Taube, Head direction cells in rats with hippocampal or overlying neocortical lesions: Evidence for impaired angular path integration. *J. Neurosci.* **19**, 7198–7211 (1999). [Medline](#)

27. H. Maaswinkel, I. Q. Whishaw, Homing with locale, taxon, and dead reckoning strategies by foraging rats: Sensory hierarchy in spatial navigation. *Behav. Brain Res.* **99**, 143–152 (1999). [Medline](#) [doi:10.1016/S0166-4328(98)00100-4](#)

28. J. A. Ainge, M. Tamosiunaite, F. Woergoetter, P. A. Dudchenko, Hippocampal CA1 place cells encode intended destination on a maze with multiple choice points. *J. Neurosci.* **27**, 9769–9779 (2007). [Medline](#) [doi:10.1523/JNEUROSCI.2011-07.2007](#)

29. J. L. Kubie, A driveable bundle of microwires for collecting single-unit data from freely-moving rats. *Physiol. Behav.* **32**, 115–118 (1984). Medline doi:10.1016/0031-9384(84)90080-5

30. S. Royer, A. Sirota, J. Patel, G. Buzsáki, Distinct representations and theta dynamics in dorsal and ventral hippocampus. *J. Neurosci.* **30**, 1777–1787 (2010). Medline doi:10.1523/JNEUROSCI.4681-09.2010

31. E. Batschelet, *Circular Statistics in Biology* (Academic Press, New York, 1981).

32. R. F. Langston, J. A. Ainge, J. J. Couey, C. B. Canto, T. L. Bjerknes, M. P. Witter, E. I. Moser, M. B. Moser, Development of the spatial representation system in the rat. *Science* **328**, 1576–1580 (2010). Medline

33. T. J. Wills, F. Cacucci, N. Burgess, J. O'Keefe, Development of the hippocampal cognitive map in preweanling rats. *Science* **328**, 1573–1576 (2010). Medline doi:10.1126/science.1188224

34. R. M. Yoder, J. S. Taube, Head direction cell activity in mice: Robust directional signal depends on intact otolith organs. *J. Neurosci.* **29**, 1061–1076 (2009). Medline doi:10.1523/JNEUROSCI.1679-08.2009

35. B. J. Clark, J. E. Brown, J. S. Taube, Head direction cell activity in the anterodorsal thalamus requires intact supragenual nuclei. *J. Neurophysiol.* **108**, 2767–2784 (2012). Medline doi:10.1152/jn.00295.2012

36. L. M. Giocomo, T. Stensola, T. Bonnevie, T. Van Cauter, M. B. Moser, E. I. Moser, Topography of head direction cells in medial entorhinal cortex. *Curr. Biol.* **24**, 252–262 (2014). Medline doi:10.1016/j.cub.2013.12.002

37. F. Sargolini, M. Fyhn, T. Hafting, B. L. McNaughton, M. P. Witter, M. B. Moser, E. I. Moser, Conjunctive representation of position, direction, and velocity in entorhinal cortex. *Science* **312**, 758–762 (2006). Medline doi:10.1126/science.1125572